

Copyright 2007, IEEE. Published in *The Proceedings of the 41<sup>st</sup> Asilomar Conference on Signals, Systems, and Computers*, Pacific Grove, CA, November 4-7, 2007.

Personal use of this material is permitted. However, permission to reprint/republish this material for advertising or promotional purposes or for creating new collective works for resale or redistribution to servers or lists, or to reuse any copyrighted component of this work in other works, must be obtained from the IEEE.

# High Resolution Optical Tracking to Identify Adhesive Events *in Vitro*

Brian J. Schmidt, Christopher D. Paschall, William H. Guilford, and Michael B. Lawrence

Department of Biomedical Engineering

University of Virginia

415 Lane Rd.

Charlottesville, VA 22908 USA

{bschmidt,cdp8x,whg2n,mbl2a}@virginia.edu

**Abstract**—Glycoproteins serve as ligands on metastatic cancer cells to mediate labile adhesive interactions with the vascular endothelium. The sub-second transience of carbohydrate-protein bonding events poses challenges for quantification of adhesion by optical tracking. We report the development of a simple, shape-based algorithm with novelty in its application to high spatiotemporal resolution tracking. We report positional and morphological signals from the spatial, time, and frequency domains for rigid particles and distensible cells. Error was comparable with previous methods: the resolution-dependent positional precision was 7 nm upon minimization of mechanical noise under experimental conditions.

## I. INTRODUCTION

Selectins are a class of biomechanically responsive adhesion molecules expressed on the vascular endothelium important for the capture and recruitment of leukocytes during their trafficking regime. In addition to leukocytes, other cell types might utilize selectin binding for recruitment to new tissues. Specifically, it has been postulated that metastatic cancer cell variants may exhibit upregulated expression of the glycosyltransferase enzymes that confer the capability bind selectins to their cell surface proteins [1].

Selectins exhibit rapid, reversible binding kinetics and anchor surfaces to within 100 nm of each other as they form bonds. Therefore, the spatial and temporal resolution of a videomicroscopy system is critical for measurements of selectin-mediated cell and microbead motion [2]. Due to differences in the binding kinetics of different glycoforms, differences in the density and localization of selectin substrates on various cell types, and differences in the morphology and mechanoresponsiveness of the cytoskeleton, different cell types may exhibit distinct, characteristic patterns of motion and shape changes when interacting with the same substrate. In addition to testing for characteristic antibody binding epitopes, as has been done with flow cytometry, it may be useful to classify cells with tracking-assisted functional cytometry [3].

To investigate the potential utility of functional cytometry, we report qualitative results for cancer cell line interactions with E- and P-selectin. A quantitative assay was also performed to characterize rigid spheres, leukocytes, and a cancer cell line interacting with P-selectin under shearing

conditions according to their patterns of motion and morphological deformation.

## II. MATERIALS AND METHOD

### A. Surface Preparation

Soluble P-selectin construct and recombinant P-selectin IgG chimera were purchased from R&D Systems. Recombinant E-Selectin IgG chimera was purchased from Glycotech. Slides were cut from untreated polystyrene tissue culture dishes and washed three times in alternating ethanol and deionized water rinses. To ensure adhesion at high wall shear rates and avoid potential activation through the Fc-receptor when testing neutrophils, 60  $\mu\text{g/mL}$  of the soluble P-selectin construct was used to coat the slides for quantitative measurement of motion-related signals. Rings were cut from microcentrifuge tubes, a 60  $\mu\text{L}$  droplet of protein solution placed in the ring, and the droplet was covered with the cap to eliminate the air-water interface and the resulting doughnut deposition pattern [3]. Adsorption was allowed to proceed for 3 hr at room temperature. The surfaces were washed with 1% Tween 20 detergent in HBSS and allowed to incubate overnight at 4  $^{\circ}\text{C}$ . Recombinant IgG construct was adsorbed at lower concentrations for a qualitative screen at low wall shear rates.

### B. Microbead and Cell Preparation

P-selectin Glycoprotein Ligand-1 (PSGL-1) was purified from HL-60 cells as described previously [4]. Polystyrene microbeads (15  $\mu\text{m}$ ) were purchased from Polysciences and coated with a 1:10 dilution of the PSGL-1 stock solution using a similar procedure as with the surfaces. MDA-MB-231 cell lines were cultured in high glucose DMEM supplemented with 10% Fetal Bovine Serum (FBS) and 1% Penicillin and Streptomycin solution (P/S). SKOV3 cell lines were cultured in McCoy's 5A Medium supplemented with 10% FBS and 1% P/S. Anchorage-dependent MDA-MB-231 and SKOV3 cells were incubated in 50 mM EDTA to detach them from the culture surfaces for evaluation in the flow chamber assay. Jurkat cells were cultured in RPMI 1640 supplemented with 10% FBS, 1% P/S, and 2 mM L-glutamine. TK-1 cells were cultured in Opti-MEM supplemented with 10% FBS, 1% P/S, and 2 mM L-glutamine. Neutrophils were isolated from

heparin-treated human blood by centrifugation at 400Xg over 1-Step Polymorphs. The flow buffer consisted of HBSS supplemented with 20 mM CaCl<sub>2</sub> and 10 mM HEPES and was 0.2- $\mu$ m filtered prior to adding the cells. For experiments with microbeads, 1% Tween 20 was added to minimize aggregate formation.

### C. Flow Cell Assay

Experiments were performed by mounting a vacuum-immobilized flow cell from Glycotech on the slides and imaging with a Nikon Eclipse TE300 microscope on an active vibration isolation table. Shearing flow was supplied with a Harvard Apparatus PhD 2000 syringe pump. Cells were qualitatively screened for binding activity by testing whether they accumulated at a low wall shear rate ( $\leq 50 \text{ s}^{-1}$ ). For quantitative measurements of cell motion with neutrophils and Jurkat cells, the wall shear rate was increased to 1,000  $\text{s}^{-1}$  after accumulation. Quantitative measurements with microbeads were limited to 300  $\text{s}^{-1}$ .

### D. Imaging and Tracking

A 40X Plan Fluor, 0.6 NA objective was used. The correction collar was adjusted for imaging through the polystyrene slide and the field and condenser diaphragms were adjusted as described elsewhere [5]. A high-speed Photron Fastcam PCI-R2 was used for image capture. The digital shutter was fixed to operate at 1 kHz for all acquisitions since this eliminated motion blur and allowed sufficient light for imaging without increasing the camera gain, which was fixed at 1X. A green interference filter was used to narrow the chromatic content of the brightfield illumination. In order to obtain satisfactory edge delineation when tracking the cells, which had a refractive index close to the buffer, the image was slightly defocused during acquisition to enhance the Becke line effect. A centroid tracking algorithm was coded in Matlab, **cmorph01**, and has been made available online at the lab website (<http://bme.virginia.edu/lawrence>). The tracking method is described in Fig. 1.

### F. Characterization of Noise

To estimate the mechanical and electronic noise of the system, microbeads were suspended in ethanol, dried to slides, and imaged under experimental conditions. Experiments flowing microbeads over non-functionalized slides were conducted to characterize the mechanical noise in the flow system.

### G. Data Analysis

From the positional noise observed when tracking fixed microbeads, we estimated the maximum rate the tracked data could be sampled at during analysis. The effect of reducing frame rate (decimation) post-acquisition on the positional error was checked. We defined the noise-limited sampling rate as:

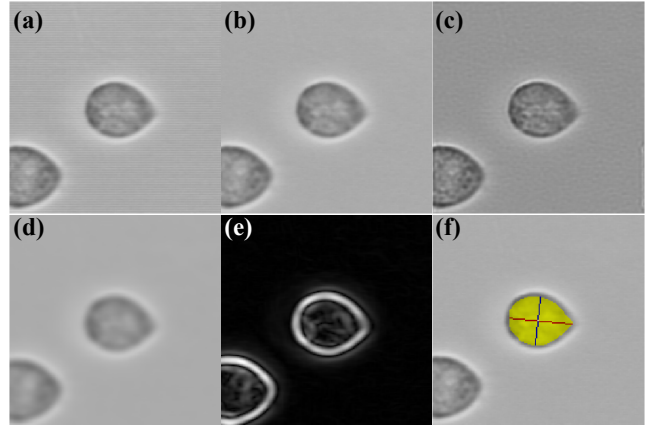


Fig. 1. Steps in the shape-based centroid tracking algorithm, **cmorph01**. (a) A subsection of the original image was loaded to speed computation. (b) The two analog-to-digital converters on the Fastcam had an apparent gain mismatch, so the image was linearly corrected by measurements taken of blank fields with varying illumination intensities. (c) Optionally, deconvolution with a measured point spread function could be performed. However, internal details of cells sometimes confused the tracking algorithm since it was looking for object edges. The deconvolution steps were omitted to save computation time and avoid this complication. (d) A spatial low-pass (averaging) filter was applied to blur internal cell details while maintaining the edges. (e) The gradient of the image was computed. Decreasing thresholds were applied to the gradient image until a ring surrounding the cell resulted in object detection when a morphological fill operation was applied at a guessed point within the object. (f) The original image was color-coded to assist in validation of the results. The centroid of the detected object was rounded to the nearest whole pixel value and shown in white. The major axis through the centroid was colored in red and the perpendicular axis was colored in blue. The color of the object was scaled between blue and red according to a jet color map based on the ratio of the length of the major to the minor axis. The ratio of these lengths was defined as the Shape Strain Index (SSI).

$$v = \frac{\epsilon_v}{3\sigma_{f\text{fip}}} \quad (1)$$

Here,  $v$  is the reduced noise-limited frame rate (fps),  $\epsilon_v$  is the acceptable error in velocity ( $\mu\text{m/s}$ ), and  $\sigma_{f\text{fip}}$  is the measured standard deviation of the frame-to-frame positional change ( $\mu\text{m}$ ) for a stationary reference (precision). Note that if subsequent measurements of position are independent and identically Gaussian distributed,

$$\sigma_{f\text{fip}} = \sqrt{2}\sigma_p, \quad (2)$$

where  $\sigma_p$  is the standard deviation in the position of the stationary reference (precision). The Nyquist criterion limited analysis of the time-frequency data to half the frame rate after decimation. We measured the signal-to-noise ratio (SNR),

$$SNR = \frac{I_{TGI}}{\sigma_{BGI}}, \quad (3)$$

where  $\sigma_{BGI}$  was the standard deviation of background intensity in the gradient image and  $I_{TGI}$  was the intensity threshold for object detection. For spatial fast Fourier analysis, a spatial grid with 10 nm increments was created to sample position data using inverse distance weighted interpolation. The flow direction has been presented as the x-direction and the perpendicular direction as the y-direction.

TABLE I  
QUALITATIVE SELECTIN BINDING SCREEN

Cell Line	Tissue Source	P-selectin Binding	E-selectin Binding
MDA-MB-468	Breast Carcinoma	Not Tested	+*
MDA-MB-231	Breast Carcinoma	-	-
SKOV3	Ovarian Carcinoma	-	-
LS174T	Colorectal Carcinoma	+ <sup>†</sup>	+ <sup>§</sup>
HL-60	Promyelocytic Leukemia	+ <sup>‡</sup>	+ <sup>‡</sup>
Jurkat	Lymphoma	+	+
TK-1	Lymphoma	-	-

\*From previous result [6]. <sup>†</sup>From [7]. <sup>‡</sup>From [8]. <sup>§</sup>From [9].

### III. RESULTS

#### A. Cell Line Screen

The results along with selected previous work were compiled in Table I. Notably, two different MDA-MB cell lines exhibited different selectin binding activity. The different selectin binding activity of different lines cloned from the same tumor source illustrates the potential utility of functional cytometry for identifying patients that have developed variants that put them at high risk for a negative clinical outcome. Surprisingly, we found Jurkat cells bound selectins well in the assay, in opposition to previous findings [10]. This may be due to clonal differences and allowing the cells to accumulate at a low wall shear rate. Additional Jurkat cells were not observed to adhere once the wall shear rate was increased to  $1,000 \text{ s}^{-1}$ .

#### B. Characterization of Noise

Electronic and mechanical noise sources were classified based on time and frequency domain signals from microbead position data. When mechanical noise was removed from the system (Fig. 2(a,c), blue lines) by drying the microbead to the slide and allowing a few minutes for the stage to settle before imaging, the remaining noise appeared to be evenly distributed about all frequencies. The residual noise was likely electronic in nature, from sources such as shot noise in the CCD. The frequency content of mechanical noise when the bead was dried to the slide agreed well with what one would expect from the resonant frequency of a vibration table ( $\sim 1\text{-}5 \text{ Hz}$ ) and was less than  $40 \text{ nm}$  in magnitude (Fig. 2(a,c), red lines). A case of significant mechanical noise in a measurement of a freely flowing bead is shown (Fig. 2(b,d), black lines). Mechanical flow noise was minimized by taping down flow lines, minimizing air bubbles in the flow lines, and using Teflon syringe plungers (Fig. 2(b,d), green lines).

To set the noise-limited sampling rate, we tracked stationary  $6\text{-}15 \text{ }\mu\text{m}$  microbeads with low mechanical noise and investigated the effect of decimation on the frame-to-frame positional precision. Systematic dependence on decimation factors between 1 and 10 was not apparent and other sources of variation likely dominated. We assumed the frame-to-frame positional precision to be independent of sampling rate with fixed shutter speed ( $1 \text{ kHz}$ ). We applied (1) using the worst  $3\sigma_{\text{dfp}}$  from four immobilized microbeads with low mechanical noise ( $0.140 \text{ pixels}$ ) to obtain a noise-limited sampling rate of

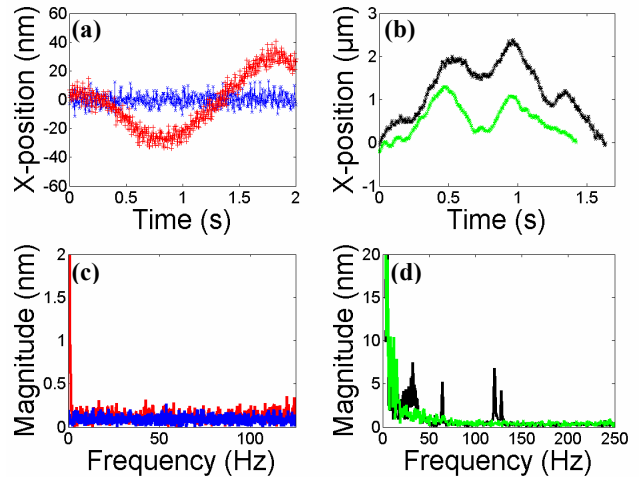


Fig. 2. Quantification and classification of noise. (a) Blue line: sample data acquired at 250 fps for a bead dried to a slide and mounted in a flow cell. Red line: mechanical noise was apparent in different trial with similar sample preparation. (b) Black line: results for a flowing microbead in a non-mechanically optimized flow system. Green line: results from a mechanically optimized system. Frames were acquired at 500 fps. To remove the average effect of motion, the x-position is shown as the x-position minus the average velocity multiplied by time. (c) Fourier transforms of (a) illustrate the distribution of noise for fixed objects. Red line: The low frequency noise was likely due to stage motion. Blue line: the low frequency noise was not apparent. (d) Black line: mechanical noise for flowing microbeads was broadly distributed below  $50 \text{ Hz}$ , notably of similar frequency to selectin bond lifetimes [2]. Note oscillations at  $32, 64,$  and  $128 \text{ Hz}$  and an additional spike at  $120 \text{ Hz}$ . Green line: peaks were not present once the flow system was optimized.

$125 \text{ fps}$  with  $3.2 \text{ }\mu\text{m/s}$  of error for round objects. The SNR for this worst case was 54. As expected, absolute precision was better, and the worst  $3\sigma_p$  value from the same dataset was  $0.113 \text{ pixels}$ . Precision could be improved for the microbeads by about 30% with deconvolution, but this step was omitted to save computation time and since it could create difficulty when tracking cells with internal features. We did not find evidence for a definitive correlation between object area ( $\text{pixels}^2$ ) and frame-to-frame precision ( $\text{pixels}$ ) over the range of object sizes tracked, but the spatial precision was noted to improve on a distance basis for the same object when tracked at  $40\times$  optical magnification as opposed  $20\times$ .

#### C. Analysis of Motion

Results for a representative microbead are shown in Fig. 3. A sample tracked image is presented in Fig. 3(a). Tracked movie sequences from the algorithm assisted validation of the results: it was possible to review color overlay movies to verify the algorithm correctly identified the object. Occasional collisions between optically focused microbeads created difficulty for the algorithm since there was no contrast where the beads touched. Microbeads passing out of the depth of field above the tracked object did not have a visible effect on the centroid location in the tracked movie sequences. Molecular bond formation events appeared to cause discrete

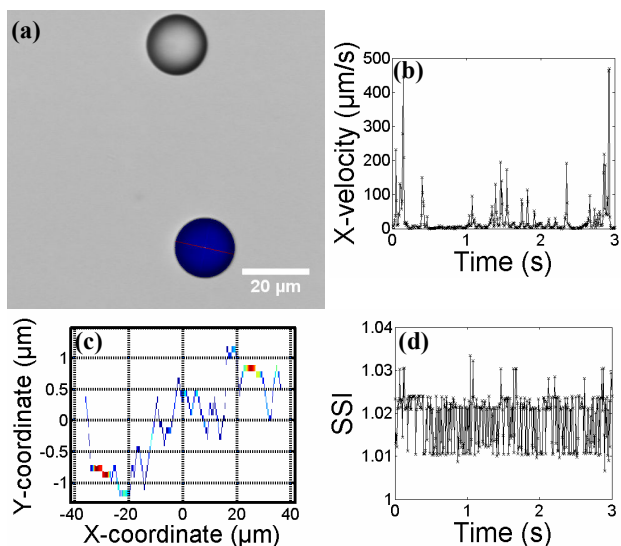


Fig. 3. Sample signals from a representative microbead. (a) Sample tracked image. (b) X-velocity as a function of time illustrates pauses. (c) X-velocity as a function of the centroid coordinates illustrates motion perpendicular to the flow direction. Color values were scaled between the extremes in (b). (d) SSI.

pauses in the motion of microbeads (Fig. 3(b)). Since previous investigations have suggested using the distance between pause events as a measure of the rebinding rate [11], the x-velocity is plotted as a function of spatial coordinates for reference in Fig 3(c). The interpolation grid for plotting was coarse to facilitate visualization in this format. The measured SSI (Shape Strain Index) was within 4% of the true value of 1 for a circle (Fig. 3(d)). Fig. 4 and 5 illustrate results for a representative neutrophil and Jurkat cell, respectively.

The temporal frequency dependence of the SSI was analyzed with fast Fourier transforms to look for patterns characteristic to the cancer cells. The result of an average of 10 objects is presented in Fig. 6. The SSI for microbeads was constant and small at nonzero frequencies, as would be expected for a rigid, symmetric particle. Neutrophils exhibited a higher SSI than microbeads at frequencies less than 3 Hz and converged on the results for microbeads at higher frequencies. These data suggested cell compliance behaved as a low pass filter for the neutrophils: force deformed neutrophils at low frequencies but not at high ones. Jurkat cell deformation remained higher than for microbeads at high frequencies, which was probably due to the irregular shape of the Jurkat relative to the other particles analyzed. The results suggested that for the Jurkat cells, the SSI was an indicator of changes in the shape of the object projection in the XY plane as the particle rotated end-over-end rather than morphological changes in the cell due to force.

Fast Fourier analysis was employed to identify general spatial motion patterns and those characteristic to the cancer cell line being investigated (Fig. 7). Notably, for all particles there was typically higher spatial frequency content in the

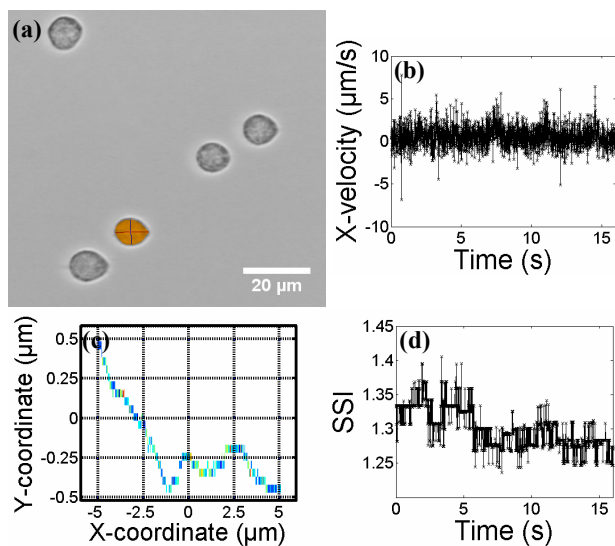


Fig. 4. Sample signals from a representative neutrophil. (a) Sample tracked image. (b) X-velocity as a function of time had a low signal to noise for the slowly moving neutrophils. (c) X-velocity as a function of the centroid coordinates. (d) SSI.

signal in the y-direction. A region of especially high spatial frequency was apparent solely for the Jurkat cells at frequencies greater than  $1 \mu\text{m}^{-1}$  in the x-direction and  $10 \mu\text{m}^{-1}$  in the y-direction. Notably, motion in both directions was correlated, but the pattern for the rigid microbeads contained isotherms oriented perpendicular to a large component seen extending at  $45^\circ$  for all three particles. Neutrophils appeared to have the highest x-direction spatial frequency content in their motion. This range of x-direction content,  $1 - 10 \mu\text{m}$ , is of a similar size as the cell, suggesting pausing caused by a second, pre-existing bond following breakage of a load-bearing bond

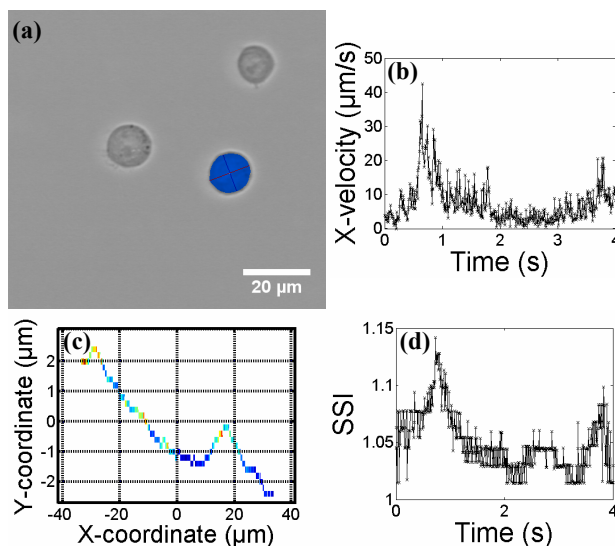


Fig. 5. Sample signals from a representative Jurkat cell. (a) Sample tracked image. (b) X-velocity as a function of time shows a lack of discretely defined pause events, in contrast to the microbeads. (c) X-velocity as a function of the centroid coordinates. (d) SSI.

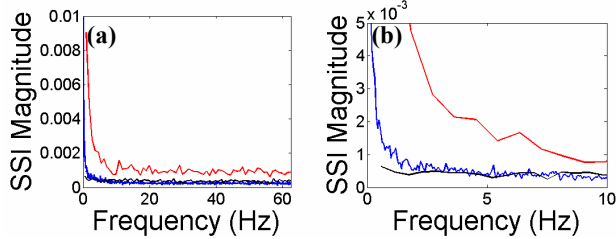


Fig. 6. Fourier transform of SSI data. Neutrophils were much sampled than the microbeads or Jurkat cells since they moved much more slowly. (a) Results for microbeads (black line), neutrophils (blue line), and Jurkat cells (red line). The DC value was omitted for clarity and was 1.02, 1.21, and 1.10, respectively. (b) The low-frequency region from (a) was expanded.

cluster. Fourier analysis illustrated clear differences in the motion patterns and a thorough study should be conducted to determine the contribution of noise in the transform, which signal characteristics might be common to cancer cells, and what new lessons can be deduced about the biophysics.

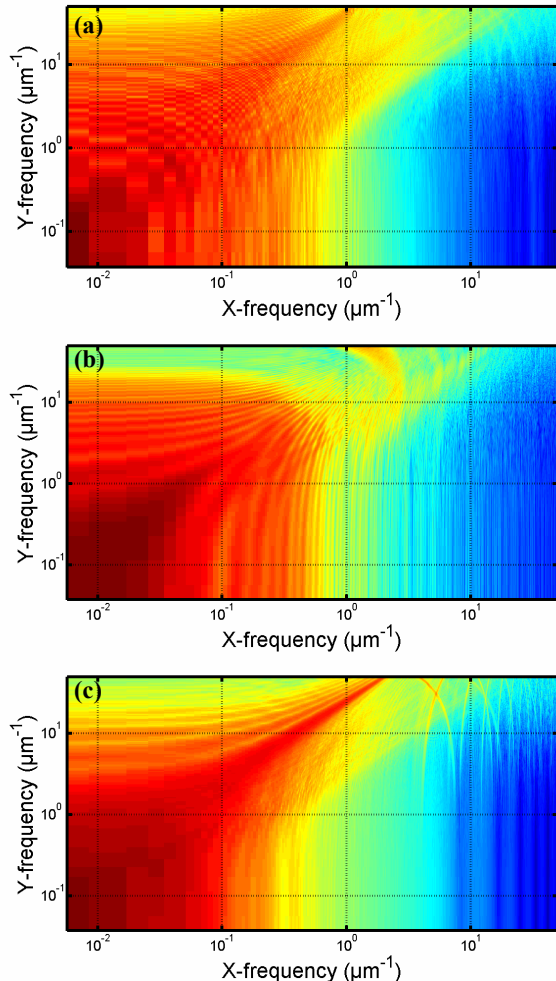


Fig. 7. Spatial Fourier transform results for x-velocity using the average of 10 particles. Results with a DC component were assigned to the first row and column of the plot. Results were converted to dB and then scaled. (a) Microbeads. (b) Neutrophils. (c) Jurkat cells.

#### IV. DISCUSSION

We report here the development of a shape-based tracking algorithm and illustrate the application to measurements of selectin-mediated cell motion with physiologic wall shear rates ( $1,000 \text{ s}^{-1}$ ). The positional precision for round objects was estimated to be 7.0 nm, or 0.038 pixels (one standard deviation). The result agreed well with a theoretical study of the precision of the centroid tracking method for similarly-sized, fluorescent particles, which found a range of 0.02 - 0.1 pixels assuming an SNR of 6-30. Although we did not explicitly investigate positional bias, the SNR was 54, and previous investigation found bias to negligible for a centroid tracking method with SNR greater than 5 [12].

#### ACKNOWLEDGMENTS

The authors would like to thank Nicole F. Brackett and José L. Tlaxca for assistance culturing the cell lines tested, Bryan R. Smith for protein isolation, and Dr. John A. Hossack for insightful conversations regarding noise detection and minimization.

#### REFERENCES

- [1] I. P. Witz, "The involvement of selectins and their ligands in tumor-progression," *Immunol Lett*, vol. 104, pp. 89-93, 2006.
- [2] M. J. Smith, E. L. Berg, and M. B. Lawrence, "A direct comparison of selectin-mediated transient, adhesive events using high temporal resolution," *Biophys J*, vol. 77, pp. 3371-83, 1999.
- [3] B. J. Schmidt, P. Huang, K. S. Breuer, and M. B. Lawrence, "A Catch Strip Assay for the Relative Assessment of Rapid, Two-Dimensional Protein Association Kinetics," *Anal Chem*, In press.
- [4] E. Y. Park, M. J. Smith, E. S. Stropp, K. R. Snapp, J. A. DiVietro, W. F. Walker, D. W. Schmidtke, S. L. Diamond, and M. B. Lawrence, "Comparison of PSGL-1 microbead and neutrophil rolling: microvillus elongation stabilizes P-selectin bond clusters," *Biophys J*, vol. 82, pp. 1835-47, 2002.
- [5] S. Inoué and K. R. Spring, *Video Microscopy: The Fundamentals*, 2nd ed. New York: Plenum Publishing Co., 1997.
- [6] C. D. Paschall, A. R. L. Gear, and M. B. Lawrence, "Metastatic potential of breast carcinoma cells correlate ability to roll on E-selectin and IL-1B stimulated endothelium," presented at The BMES Annual Fall Meeting, Philadelphia, PA, 2003.
- [7] W. D. Hanley, S. L. Napier, M. M. Burdick, R. L. Schnaar, R. Sackstein, and K. Konstantopoulos, "Variant isoforms of CD44 are P- and L-selectin ligands on colon carcinoma cells," *Faseb J*, vol. 20, pp. 337-9, 2006.
- [8] W. D. Hanley, M. M. Burdick, K. Konstantopoulos, and R. Sackstein, "CD44 on LS174T colon carcinoma cells possesses E-selectin ligand activity," *Cancer Res*, vol. 65, pp. 5812-7, 2005.
- [9] M. B. Lawrence, G. S. Kansas, E. J. Kunkel, and K. Ley, "Threshold levels of fluid shear promote leukocyte adhesion through selectins (CD62L,P,E)," *J Cell Biol*, vol. 136, pp. 717-27, 1997.
- [10] R. N. Knibbs, R. A. Craig, S. Natsuka, A. Chang, M. Cameron, J. B. Lowe, and L. M. Stoolman, "The fucosyltransferase FucT-VII regulates E-selectin ligand synthesis in human T cells," *J Cell Biol*, vol. 133, pp. 911-20, 1996.
- [11] C. D. Paschall, W. H. Guilford, and M. B. Lawrence, "Enhancement of L-selectin, but not P-selectin, Bond Formation Frequency by Convective Flow," *Biophys J*, vol. In Press, 2007.
- [12] M. K. Cheezum, W. F. Walker, and W. H. Guilford, "Quantitative comparison of algorithms for tracking single fluorescent particles," *Biophys J*, vol. 81, pp. 2378-88, 2001.